Title

Superresolution Imaging Reveals the Spatial Organization of CD81 Microdomains in Regulating Membrane Signaling on Jurkat T Cell Microvilli

Authors

Neal T. Ramseier[1], Haoran Jing[1], Jesse Anderson[2], Ying S. Hu[1]*

Affiliations

[1]Department of Chemistry, College of Liberal Arts and Sciences, University of Illinois Chicago, Chicago, IL 60607, USA

[2]Department of Chemical Engineering, College of Engineering, University of Illinois Chicago, Chicago, IL 60607, USA

*Corresponding Author. Email: yshu@uic.edu

Abstract

Tetraspanin proteins are closely associated with high-curvature membrane structures and play key roles in organizing membrane domains and regulating membrane signaling in immune cells. However, their specific roles in regulating T-cell membrane signaling, particularly within the microvilli often characteristic of these cells, remain poorly understood. Here, we used Jurkat T cells as a model system and investigated CD81 as a membrane of the tetraspanin family. Using total internal reflection fluorescence (TIRF) microscopy and structured illumination microscopy (SIM), we identified an enrichment of the tetraspanin CD81 microdomains along the actin-rich membrane microvilli. At the tip of the microvilli, SIM images revealed the spatial colocalization of CD81 with T cell receptors (TCR) and CD63, implying a potential role for CD81 in regulating TCR signaling in conjunction with CD63. Spatial analysis of CD81 and CD63 microdomains from the dual-color SIM data revealed their preference for associating with each other. Cluster analysis of direct stochastic optical reconstruction microscopy (*d*STORM) data revealed that *in vitro* T cell activation results in reduced domain sizes and increased domain separation of CD81. These findings provide visual evidence of the spatial organization and rearrangement of CD81 on the T cell microvilli, highlighting its potential role in signal regulation on specialized membrane protrusions.

MAIN TEXT

Introduction

Tetraspanins are membrane proteins that associate with each other to form tetraspanin-enriched microdomains (TEMs) on the plasma membrane, playing key roles in the organization of the membrane architecture (*1–3*). CD81 represents a tetraspanin protein consisting of four transmembrane domains and is localized in TEM on the cell surface. CD81 mediates numerous cellular functions, including cellular adhesion, intracellular signaling, proliferation, and regulation of T-cell morphology (*4*, *5*). In addition, CD81 has been reported to localize on the microvilli in endothelial cells (*6*) and is known for regulating membrane protrusions (*7*). CD81 has been demonstrated to localize on the microvilli of B cells and monocytes and play a role in microvilli regulation in primary mouse peripheral blood mononuclear cells (*7*).

In T cells, membrane microvilli are dynamic, actin-associated structures that facilitate environmental probing and sensing (*8–10*). The enrichment of signaling proteins allows microvilli to survey antigens on antigen-presenting cells and form complexes for subsequent signaling processes (*11–13*). The signaling function of T cell microvilli is suggested by the clustering of T cell receptors (*12–14*), as well as the release of T cell microvilli particles (TMP) containing adhesion molecules and cytokines (*11*, *15*, *16*). Given the known association of tetraspanins with high-curvature membrane structures, understanding the nanoscale spatial organizations of tetraspanin proteins on the microvilli enhances our understanding of the signaling regulation mechanism at these specialized membrane structures.

Electron microscopy (EM) immunogold staining has revealed the presence of CD81 on Jurkat T cell microvilli (*17*). CD81 has been reported to regulate T-cell activation (*18–20*) and is known to associate with CD4 and CD8 (*21*, *22*). Moreover, CD81 has been shown to act as a costimulatory molecule to activate T cells when stimulated with CD3 (*23–25*). While these studies point to the potential role of signal regulation, the nanoscale distribution and spatial arrangements of CD81 concerning other membrane proteins on the microvilli have not been visualized. Such information enhances the understanding of T-cell signaling in specialized membrane protrusions.

In this study, we employed fluorescence and superresolution imaging to examine the spatial distribution of the CD81. We observed a CD81 enrichment with TEMs on Jurkat T cell microvilli. We investigated the spatial relationship of CD81 with T cell receptors (TCR) and CD63 along and on the tip of microvilli. We further revealed the ultrastructure of CD81 TEMs and their spatial redistribution upon *in vitro* activation.

Results

CD81 enrichment on T cell microvilli revealed by fluorescence and superresolution imaging.

To assess the localization of CD81 on the microvilli, we immobilized and fixed Jurkat T cells, then co-stained CD81 and F-actin with phalloidin. F-actin has been shown to be involved in the formation of cytoskeletal protrusions in T cells (*11*, *12*), dendritic cells (*26*), and other cell types (*27*, *28*). **Figure 1A** displays total internal reflection fluorescence (TIRF) images of CD81 and F-actin colocalizing on microvilli structures protruding from Jurkat cells. The F-actin distribution shows a preference toward the periphery of the cell, in conjunction with CD81. The peripheral F-actin distribution is consistent with previous reports of F-actin staining on T cells (*9*). The magnified views of the microvilli suggest a punctated distribution of CD81 compared to the continuous appearance of f-actin, revealing the presence of CD81 TEMs on the microvilli. CD81 is localized both on and next to the actin fibers.

To obtain higher spatial resolution, we performed structured illumination microscopy (DeepSIM from CrestOptics) and confirmed the distribution of CD81 clusters along the microvilli (**Figure 1B**). In contrast, the intracellular distribution of CD81 was much lower. Colocalization analysis using the intensity correlation quotient (ICQ) (*29*) revealed an ICQ value of 0.190 ± 0.017 (mean ± SD, $n = 15$) for the microvilli (**Figure S1**), suggesting a positive correlation between CD81

and F-actin. High-magnification views in **Figure 1B** further revealed the segmented TEMs of CD81, which was identified on the microvilli of most of the Jurkat cells. Furthermore, the higher resolution revealed non-consistent localization of CD81 in the context of F-actin, where CD81 is localized on top of (**Figure 1C1**), next to (**Figure 1C2**), and wrapping around (**Figure 1C3**) the F-actin fibers. While CD81 was revealed on the microvilli near the immobilizing surface, we employed volumetric DeepSIM imaging and observed the prevalence of CD81-enriched microvilli across the entire T cell surface **(Figure S2**).

We observed CD81 TEMs on the microvilli with or without membrane permeabilization. Previous reports have shown tetraspanins to remain associated under non-stringent detergent conditions (*30*, *31*). A comparison between fixatives (4% paraformaldehyde (PFA) or 4% PFA + 0.1% glutaraldehyde (GA)) with and without permeabilization using saponin all revealed similar phenotypes of CD81 intensity variation along the microvilli (**Figure S3**). The observation of this phenotype in all four conditions suggests the segmented distribution of CD81 is not due to permeabilization agents washing away the membrane enclosing the microvilli. The heterogeneous distribution of CD81 signal intensity along the microvilli suggests the spatial clustering of CD81 molecules into TEMs.

TCR is spatially associated with CD81 TEMs on the microvilli.

CD81 is known to regulate TCR signaling (*20*). Considering the observed enrichment of CD81 at the microvilli and previously reported accumulation of TCRs on and at the tips of microvilli (*11*, *13*, *14*, *32*), we investigated the spatial relationship between these two proteins. The dual-color SIM image of Jurkat cells immunostained for CD81 (green) and TCRs (blue) in **Figure 2A** revealed TCR localization throughout the Jurkat cell periphery and on the microvilli. The TCR staining presents as punctated domains on the microvilli. Notably, the magnified views of microvilli in **Figures 2B** displayed strong colocalization (teal) of TCRs with CD81 along the microvilli stalk and at the microvilli tips. The white arrows in **Figure 2B** point to locations where both CD81 and TCR puncta are observed on one of the microvilli. The observed colocalization of CD81 and TCR on the microvilli suggest a strong correlation between the spatial distribution of these two proteins.

The line profiles in **Figure 2C** confirm the spatial correlation between TCR with CD81 along the microvilli, indicating a strong association between CD81 and TCR. The TCR puncta on the microvilli are associated with CD81 puncta, denoted as + on the line profile, while not all CD81 puncta are associated with TCR, denoted at – on the line profile, displaying the preference of TCRs to localize with CD81. These results demonstrate a close spatial relationship between TCR puncta with CD81 TEMs, suggesting that CD81's proximity to the TCR facilitates its regulatory role in T cell activation. The physical proximity of CD81 to TCR further supports CD81's role in organizing signaling platforms on the microvilli surface.

CD63 TEMs associate with CD81 TEMs on the microvilli and TCR + CD81 at microvilli tips.

We investigated CD63 in the context of CD81 on the T cell microvilli, as tetraspanins are known to associate with one another to form TEMs (*33*). CD63 has been observed to be present on micro-protrusions in activated platelets (*34*). Additionally, CD63, like CD81, has been reported to be involved in T cell activation and can be used as a costimulatory target for activation with CD3 (*23*, *35*). SIM images of co-stained CD81 and CD63 revealed CD63 presents as punctated domains and is not as abundant as CD81 on the Jurkat T cells (**Figure 3A**). We observed a preference of CD63 association with CD81 toward the periphery of the cell, including the microvilli. Interestingly, CD63 puncta were observed at the tips of several microvilli colocalized with CD81, seen in the magnified views of **Figure 3A**. We further observe CD81 puncta colocalized with CD63, as well as CD81 or CD63 puncta not colocalized the other. The line profiles in **Figure 3B** shows the relative intensity of CD63 and CD81, with a CD63 peak at the tip of the microvilli colocalizing

with CD81. The tips of the microvilli show both slightly offset peaks of CD81 and CD63 intensity (**Figure 3B1, 3**) and fully overlapping peaks (**Figure 3B2**), indicating potential intermixing of TEMs and separate islands of CD81 and CD63 TEMs. Taken together, these observations indicate a strong spatial association of CD81 TEMs with CD63 on the microvilli, particularly at the tips of the microvilli.

We further quantitatively characterized the spatial relationship between CD81 and CD63. We analyzed the nearest neighbor distance (NND) between intensity maxima of CD63 and CD81, comparing CD63 to CD81, CD81 to CD63, CD81 to CD81, and CD63 to CD63 (**Figure S4**). Interestingly, we observed that the peaks of CD81 are closer to the peaks of CD63 than to other peaks of CD81, and the peaks of CD63 are similarly closer to CD81 peaks than to other peaks of CD63 (**Figure 3C, S5**). The difference in distance between CD81 or CD63 to itself and the other was found to be statistically significant ($n = 28$, $p < 0.0001$) using a Student's *t*-test. These results suggest a close spatial relationship between CD81 and CD63. The histograms of the total compiled NND values in **Figure 3D** further visualize this phenomenon. Moreover, both CD81 to CD63 and CD63 to CD81 display a decreasing relative frequency as the NND values increase, while CD81 to CD81 and CD63 to CD63 relative frequencies display a more normal distribution, peaking at around the mean value (**Figure 3D**). These findings indicate a strong correlation between the organization of CD63 and CD81 on the microvilli and cell periphery. Colocalization analysis of the cells further supports this notion with a calculated ICQ value of 0.334 ± 0.042 (mean ± SD, $n = 28$).

Given the colocalization of CD81 with CD63 at the tips of microvilli and the shown colocalization of CD81 with the TCR, we immunostained Jurkat cells for CD81 (green), CD63 (red), and TCR (blue). The DeepSIM image in **Figure 3E** revealed strong colocalization (white) between all three proteins at the microvilli tips (**Figure 3F**). The magnified views on the right and the line profiles in **Figure 3G** further display this colocalization of all three proteins at the tips of the microvilli. Interestingly, as in **Figure 3B**, we observe both highly aligned colocalization peaks (**Figure 3G1**) and slightly offset colocalization (**Figure 3G2**) peaks in the line profile. These shifts are shown in both the lateral and horizontal direction, indicating relevance to the organization of these domains with one another. Taken all together, these results suggest a close spatial relationship between CD81, CD63, and the TCR, providing visual evidence of CD81 and CD63's cooperative roles in regulating T cell activation on the microvilli surface through physical proximity.

_d_STORM reveals spatial rearrangements of CD81 TEMs across the microvilli after _in vitro_ activation.

We employed *d*STORM (*36*, *37*) to examine the nanoscale ultrastructure of CD81 TEMs on Jurkat T cell microvilli. Jurkat cells were landed and immobilized on a poly-L-lysine (PLL)-coated surface, then immunostained for CD81 (**Figure 4A**). **Figure 4B** presents a *d*STORM image of CD81 on a control Jurkat cell. The accumulation of CD81 localizations at the periphery of the cell, particularly along the microvilli, is shown in the magnified views in **Figure 4B**. We observed non-uniform distributions of CD81, consistent with the DeepSIM data. The high resolution of *d*STORM enables the measurement of the microvilli width (**Figure 4C**), where we found most microvilli were in the range of 100-300 nm (**Figure 4D**). This observation is consistent with previous literature, factoring in the antibody size and localization precision (*38*).

Given CD81's role in T cell activation and signaling regulation, we assessed the extent to which *in vitro* activation influences the CD81 nanoscale ultrastructure. A previous study found *in vitro* activation results in an immediate reduction in CD81 expression on the cell surface with an over 50 % decrease at 24 hours (*17*) using flow cytometry. To observe the maximal difference in CD81 surface expression due to activation, we incubated Jurkat T cells with ImmunoCult™ for 24 hours. The treated cells were landed and immobilized on a PLL-coated surface, then fixed, immunostained for CD81, and imaged by *d*STORM (**Figure 4E)**. Compared to the control cell, 24-h ImmunoCult™-activated cells displayed sparser CD81 localization densities along the microvilli

(**Figure 4F**). The magnified views of the microvilli in **Figure 4F** compared to **Figure 4B** further highlight this difference. The differential CD81 distribution was validated with SIM images of CD81 on control and 24-h activated Jurkat cells (**Figure S6**). We further confirmed the presence of microvilli on the activated Jurkat cells using a membrane dye (**Figure S7**).

To quantitatively analyze the clustering, we employed a density-based spatial clustering for applications with noise (DBSCAN) (*39*) algorithm to identify individual clusters of CD81 (**Figures 4G,H**). The magnified views of the control cell (**Figure 4I,K**) and 24-h activated cell (**Figure 4J,L**) display a difference in cluster sparsity between the two conditions. To this end, we quantified the microvilli CD81 clusters' NND. We included only clusters on the microvilli (**Figure S8, S9**) and calculated the mean cluster NND from each cell for comparison. In activated cells ($n = 6$), the mean NND significantly increased compared to control cell ($n = 6$, $p = 0.0328$) (**Figure 4M**). These results quantitatively confirm the increased sparsity of clusters after activation. The higher-magnification views in **Figures 4K, L** indicate smaller CD81 clusters after activation. To quantify the observed difference in cluster size, we calculated the maximum diameter (MD) of each cluster along the microvilli, defined as the maximum distance between two points within a cluster, as well as the total area of each cluster bounded by the outer points. The mean MD of the clusters from each cell in the control and 24-h activated showed a decrease after activation, found statistically significant ($p = 0.0007$) **(Figure 4N)**. The decrease in cluster size after activation is confirmed by an observed decrease in cluster area, also found statistically significant ($p = 0.0008$) (**Figure 4O**). Taken together, the cluster analysis of the *d*STORM images of control and activated cells indicate a spatial rearrangement of CD81 on the microvilli following activation and provide further detail of the ultrastructure of CD81 TEMs on Jurkat T cell microvilli.

Discussion

We observed an enrichment of CD81 and colocalization with F-actin at the microvilli, confirming its designation as a T cell microvilli biomarker. The "hot spots" observed in the DeepSIM images correlate to the areas with larger clusters or multiple clusters in close proximity seen in the DBSCAN analysis. These areas of high CD81 fluorescence intensity and localization density could likely be attributed to the organization of CD81 into microdomains on the membrane known as TEMs (*40*, *41*), and tetraspanins have been shown to regulate spatiotemporal distributions of membrane proteins to regulate immune cell signaling (*42*). Of note is that TEMs are not unique to T cells and are found in different cell types (*43*, *44*). CD81 in various cell types has been implicated in viral infection, including human immunodeficiency virus (*44*), Influenza (*45*, *46*), and Hepatitis C (*47*, *48*). Influenza viral budding occurs in membrane regions highly enriched with CD81, which may utilize a mechanism similar to the release of certain EVs, particularly microvesicles, from cells (*11*, *17*).

CD81 has been shown to regulate the signaling regarding the TCR (*18*, *19*). Previous studies reported CD81 internalization after activation (*17*) and the migration of CD81 to the immunological synapse (IS) during its formation (*18*, *49*). The past findings, in addition to our observations of CD81 colocalizing with the TCR on the microvilli, strongly implicate CD81 as a regulator of T-cell activation. Our observation of CD63 colocalized with CD81 at the tips of microvilli, in addition to its role as a costimulatory molecule (*35*), implicates CD63 in the signaling regulation of T cell activation (**Figure 5A**). The exact role of CD63 in T cell activation signaling is unclear; however, its localization with CD81 and the TCR provides direct evidence of spatial association between these molecules. As CD63 can serve as a costimulatory molecule for T cell activation, it is likely the localization would be near the TCR. The presence of both CD81 and CD63 further suggests the formation of TEMs at the tips of microvilli where TCR is enriched. Future studies looking into other proteins within these domains would provide further insight into the exact organization of the microvilli around TCR.

In the Jurkat T cells we imaged, the distribution of CD81 on the microvilli of CD3/CD28 treated cells appeared sparser than the microvilli of the control Jurkat cells (**Figure 5B**). Quantitative analysis of CD81 clusters identified using DBSCAN revealed smaller clusters and a sparser distribution of clusters on the microvilli of 24-h activated cells compared to control cells. This observation is consistent with a previous report noting a rapid decrease in surface CD81 expression, measured with flow cytometry after treatment with CD3 and CD28 (17). The observed decrease in CD81 density on the Jurkat T cell microvilli may be linked to its role as a regulatory molecule regarding the TCR. CD81 was shown to suppress T cell signaling, likely acting as a safety mechanism for accidental triggering (*19*), in addition to acting as a co-stimulatory molecule to TCR stimulation (*24*). After 24-h of activation, this regulatory and stimulatory mechanism may no longer be needed as the needs of the cell change, as indicated by a reduction in CD81 mRNA levels after 9-h of activation (*17*). The spatial reorganization of CD81 on the T cell microvilli in response to T cell activation suggests that specialized membrane protrusions are involved in receptor-mediated signaling and potentially downstream signaling cascade. Specifically, the enrichment of CD81, its previously reported role in T cell activation, and the enrichment of TCR on the microvilli suggest the microvilli as the major signaling hub for T cell activation. The presence of CD63 at the microvilli tips and its known role as a costimulatory molecule further supports this concept.

Limitations of our study include the use of Jurkat T cells as a model system and the cells' attachment to the glass surface. The cellular attachment to the surface and the absence of a permeabilization agent may affect the accessibility of antibodies to the membrane and microvilli directly underneath the cell. Future studies employing live-cell imaging with fluorescent proteins fused to CD81 could provide further insights into the spatial distribution of CD81 in the context of the temporal behavior of T cell microvilli, as microvilli are dynamic structures. Further studies to determine the exact roles of CD81 and CD63 in T cell activation and signaling will provide more insight into the roles of tetraspanins in regulating the T cell plasma membrane.

In conclusion, we identified CD81 as a microvilli marker in Jurkat T cells through its enrichment on these membrane protrusions. CD81 TEMs colocalize with TCRs along the microvilli, and with CD63 and TCRs at the microvilli tips, providing evidence of CD81's involvement in regulating T cell activation with CD63. The *d*STORM clustering analysis provides a quantitative understanding of the spatial redistribution of CD81 following T cell activation. These results suggest CD81 as a regulator of T cell activation signaling through a spatial association.

Materials and Methods

Reagents

Fetal Bovine Serum (F0926-500ML), tris(hydroxymethyl)aminomethane (252859-500G), sodium chloride (S3014-1KG), D-(+)-Glucose (G8270-1KG0), glucose oxidase from *Aspergillus niger* (G7141-50KU), catalase from bovine liver (C40-100MG), 0.01% Poly-L-Lysine Solution (P4707-50ML) and 2-mercaptoethanol (M6250-100ML), saponin (S-4521) were purchased from MilliporeSigma. RPMI (11875093), penicillin-streptomycin (15140-122-100 mL), DPBS (14190-144-500 mL), Cellvis chambered cover glass (C8-1-N), goat serum New Zealand origin (16210064), mouse monoclonal CD81 antibody (10630D), mouse monoclonal CD63 Alexa Fluor™ 488 antibody (MA5-18149), goat-anti-mouse IgG Superclonal™ Alexa Fluor™ 647 antibody (A28181), goat-anti-mouse IgG Superclonal™ Alexa Fluor™ 488 antibody (A28175), goat-anti-mouse IgG Superclonal™ Alexa Fluor™ 555 antibody (A28180), Bovine serum albumin (BSA, BP1600-100), Vybrant™ DiD Cell Labeling Solution (V22887), and Phalloidin Alexa Fluor™ 647 (A22287) were purchased from Thermo Fisher Scientific. Mouse monoclonal TCR α/β Alexa Fluor™ 647 (306714) was purchased from BioLegend. Ethanol (2701G) was purchased from Decon Laboratories Inc. Paraformaldehyde (15710) and glutaraldehyde (16120) were purchased from Electron Microscopy Sciences. Unconjugated gold colloids (15711–20) were

purchased from Ted Pella Inc. ImmunoCult™ Human CD3/CD28 T Cell Activator (10971) was purchased from STEMCELL Technologies.

Buffers

The following buffers were used for this study. Fixation Buffer: 4% PFA and 0.1% GA in 1x PBS. Post-Fixation Buffer: 4% PFA in 1x PBS. Saponin Wash Buffer: 0.5 % normal goat serum (NGS) and 0.005% saponin in 1x PBS. *d*STORM Buffer: 9.8% (w/v) glucose, 34 µg mL^{-1} catalase, 556 µg mL^{-1} glucose oxidase, 143 mM 2-mercaptoethanol, 50 mM Tris, and 10 mM sodium chloride.

Cell Culture

Jurkat E6-1 cells (ATCC TIB-152) were cultured in RPMI with 10% Fetal Bovine Serum (FBS) and 100 units/mL penicillin-streptomycin. The cells were kept in a humidified incubator at 37°C supplemented with 5% CO_2 and split at confluency.

Sample Preparation

Jurkat Activation

200,000 cells were added into a well of a 24-well plate. 5 µL of ImmunoCult™ Human CD3/CD28 T Cell Activator was added to the solution in 200 µL of media containing the cells. The cells were left to incubate for 24 hours in a humidified incubator at 37°C supplemented with 5% CO_2.

Cell Landing

Chambered coverglass wells were coated with 0.01 % Poly-L-Lysine. 50,000 cells were counted and resuspended in PBS. Cells were added to the chambered coverglass wells and incubated for 30 min at 37°C and 5% CO_2.

Fixation and Blocking

The landed cells were fixed in 200 µL of fixation buffer warmed to 37°C for 15 min. The cells were then washed three times with PBS. The cells were blocked and 10% NGS for 1 hour at room temperature. For F-actin and CD81 co-staining, cells were blocked and permeabilized with 0.1% saponin in 10% NGS for 1 hour at room temperature.

Immunofluorescence Staining

For single-color CD81 imaging, the cells were primary stained with 10 µg mL^{-1} mouse anti-CD81 in 10% NGS overnight in a humid chamber at 4°C. The cells were washed three times with 1x PBS for 5 minutes. The cells were secondary stained with 5 µg mL^{-1} goat anti-mouse Superclonal Alexa Fluor™ 647 in 10% NGS for 2 hours in a covered humid chamber at room temperature. Following the staining, the cells were washed four times with the 1x PBS. The cells were post-fixed in the post-fixation buffer for 5 minutes, then washed three times with 1x PBS.

For dual-color F-actin and CD81 staining, the cells were primary stained with 10 µg mL^{-1} mouse anti-CD81 in 10% NGS with 0.1% saponin overnight in a humid chamber at 4°C. The cells were washed three times with the saponin wash buffer for 5 minutes. The cells were secondary stained with 5 µg mL^{-1} goat anti-mouse Superclonal™ Alexa Fluor™ 488 in 10% NGS with 0.1% saponin for 2 hours in a covered humid chamber at room temperature. Following the staining, the cells were washed four times with the saponin wash buffer. The cells were post-fixed in the post-fixation buffer for 5 minutes, then washed three times with 1x PBS. The cells were then incubated in 167 nM Phalloidin-Alexa Fluor™ 647 in 10% NGS with 0.1% saponin overnight in a humid chamber at 4°C.

For CD81 and CD63 staining, cells were primary stained with 5 µg mL^{-1} mouse anti-CD81 in 10% NGS overnight in a humid chamber at 4°C. The cells were washed three times with 1x PBS for 5 minutes. The cells were secondary stained with 2.5 µg mL^{-1} goat anti-mouse Superclonal Alexa Fluor™ 647 in 10% NGS for 2 hours in a covered humid chamber at room temperature. Following the staining, the cells were washed four times with the 1x PBS. The cells were post-fixed in the post-fixation buffer for 5 minutes, then washed three times with 1x PBS. The cells were then incubated with 1:100 dilution of mouse-anti-CD63-Alexa Fluor™ 488 overnight at 4°C. The cells were washed three times with 1x PBS for 5 minutes.

For CD81, CD63, and TCR staining, cells were primary with 5 µg mL^{-1} mouse anti-CD81 in 10% NGS overnight in a humid chamber at 4°C. The cells were washed three times with 1x PBS for 5 minutes. The cells were secondary stained with 2.5 µg mL^{-1} goat anti-mouse Superclonal Alexa Fluor™ 647 in 10% NGS for 2 hours in a covered humid chamber at room temperature. Following the staining, the cells were washed four times with the 1x PBS. The cells were post-fixed in the post-fixation buffer for 5 minutes, then washed three times with 1x PBS. The cells were then incubated with 1:100 dilution of mouse-anti-CD63-Alexa Fluor™ 488 overnight at 4°C. The cells were washed three times with 1x PBS for 5 minutes. The cells were then incubated with 2 µg mL^{-1} mouse-anti-TCR-Alexa Fluor™ 647 antibody for 4 hours at room temperature. Following the staining, the cells were washed four times with the 1x PBS.

For membrane staining of control and activated cells, manufacturer's directions of Vybrant™ DiD Cell Labeling Solution were followed. Cells were then landed on a PLL surface and allowed to attach to the surface for 20 minutes prior to imaging.

<u>Microscopy</u>

TIRF

TIRF microscopy imaging was performed on a Nikon Ti-2 Eclipse inverted microscope coupled with NIS-Elements Advanced Research software for acquisition. A Nikon 100x/1.49 oil immersion objective was combined with 1.5x external magnification to get an effective pixel size of 73 nm. Images were captured in the 488 nm (72 W cm^{-2}) and 640 nm (20 W cm^{-2}) channels with a Prime 95B sCMOS camera (Serial Number: A18B203004). Images were acquired with a 50 ms exposure time and 16-bit data depth at ~25°C.

DeepSIM

DeepSIM images were acquired using a Nikon Ti-2 Eclipse inverted microscope equipped with a CrestOptics DeepSIM imaging system, a Nikon 60x/1.42 oil immersion objective, and a Kinetix sCMOS camera (Serial Number: A23H723002). NIS-Elements Advanced Research software (Version: 5.42.04) was used for acquisition.

For CD81 and F-actin imaging, the bottom 2 µm of the cell was imaged with a step size of 0.2 µm. The 488 nm and 640 nm laser lines were used with camera exposure times of 200 ms and 50 ms, respectively. All acquisitions utilized the standard imaging mode at room temperature.

For the full-cell volumetric imaging of CD81, 10-14 µm of the cell was imaged using a step size of 0.5 µm. The 640 nm laser lines was used with camera exposure time of 50 ms. All acquisitions utilized the standard imaging mode at room temperature.

For all CD81, CD63, and TCR imaging, only the bottom of the cell was imaged in one plane. The 488 nm, 561 nm, and 640 nm laser lines were used with integration times of 200 ms, 90 ms, and 200 ms, respectively. All acquisitions utilized the Deep imaging mode at room temperature.

400
401 *dSTORM*
402 *d*STORM imaging was performed on a Nikon Ti-2 Eclipse inverted microscope coupled with NIS-
403 Elements Advanced Research software (Version 5.21.03) for acquisition. A Nikon 100x/1.49 oil
404 immersion objective was combined with 1.5x external magnification. A Prime 95B sCMOS camera
405 (Serial Number: A18B203004) was set to 16-bit data depth and 2x2 pixel binning to create a pixel
406 size of 147 nm. Exposure time was set to 20 ms. A region of interest (ROI) of 512x512 pixels
407 (256x256 after binning) was selected. Gold colloids were added prior to imaging as fiducial markers
408 for drift correction. *d*STORM buffer was added into the well of the sample and sealed with parafilm.
409 *d*STORM images were acquired using a 640 nm laser with a measured power density of ~5 kW cm^{-}
410 ^{2} after the objective. 405 nm laser was gradually increased to maintain adequate blinking. 70,000
411 image frames were obtained at room temperature.
412
413 Data Processing
414 *Image Reconstructions*
415 DeepSIM images were reconstructed from the raw data using the Nikon Elements Advanced
416 Research (Version: 5.42.04) software along with the DeepSIM software addition. The reconstructed
417 images (.nd2 file format) were saved and opened in Fiji. For F-actin and CD81 imaging, a Z-
418 projection of all the Z-slices was performed to create a 2D representation of the images.
419
420 *d*STORM image reconstruction was performed using the Fiji plugin ThunderSTORM (*50*). Drift
421 correction for T cell imaging was performed using gold nanoparticle fiducial markers. Localized
422 single-molecule events with a localization uncertainty greater than 20 nm and sigma (standard
423 deviation of the integrated Gaussian localization function) greater than 200 nm were filtered out
424 from the analysis. The visualizations shown are normalized Gaussian with a pixel size of 20 nm.
425 No nonlinear or partial image adjustments were performed.
426
427 *Colocalization Analysis*
428 Colocalization analysis was performed in Fiji using the Coloc2 plugin. The background was
429 subtracted using an area outside the cell. ROIs were drawn around the areas of interest. The intensity
430 correlation quotients (ICQ) were calculated and stored in an Excel file.
431
432 *Maxima NND analysis*
433 The images of CD81 and CD63 were compiled, and an ROI was drawn to include only the
434 periphery of the cell, mainly including the microvilli. ImageJ was used to find the maxima in the
435 images of both channels separately. The list was exported in the .csv file format. A custom
436 MATLAB code was employed to calculate the minimum distance between the points. Only non-
437 zero distances were considered for the data sets calculating the CD81 to CD81 and CD63 to
438 CD63 NNDs. All values were compiled by cell for the intracellular comparison, or all together for
439 the histogram visualization.
440
441 *DBSCAN Clustering Analysis*
442 Sections of microvilli from the cells were cropped to isolate x-y coordinate localizations from the
443 *d*STORM reconstruction. The x-y coordinates for each cell's microvilli were then compiled.
444 DBSCAN analysis was performed using a custom-written MATLAB code that uses the DBSCAN
445 clustering algorithm to cluster the *d*STORM coordinates. The DBSCAN clustering parameters were
446 set to a minimum number of points = 7 and a search radius (Epsilon) = 10. Each cluster identified
447 by DBSCAN had its nearest neighbor distance calculated by comparing the distance of the centroid
448 of the cluster to the centroids of the other clusters in the data set and finding the minimum value.
449 Each cluster's maximum diameter was calculated by finding the distance between each point in the

cluster and finding the maximum value. Area was calculated using boundary function in MATLAB to create a boundary around the cluster and calculating its area. NND, MD, and area values for each cluster were compiled and exported for analysis.

Statistical Analysis

Two-tailed Student's T-tests were performed to assess statistical significance in GraphPad Prism.

Acknowledgments

The authors thank Hirushi Gunasekara for her valuable comments and assistance in editing the manuscript.

Funding:

Research reported in this publication was supported by the National Institute of General Medical Sciences of the National Institutes of Health under Award Number R35GM146786 (YSH) and the College of Liberal Arts and Sciences, University of Illinois Chicago. The content is solely the responsibility of the authors and does not necessarily represent the official views of the National Institutes of Health.

Author contributions:

Conceptualization: YSH, NTR, HJ
Methodology: NTR, HJ, JA
Investigation: NTR
Visualization: NTR
Writing—original draft: NTR
Writing—review & editing: NTR, YSH, HJ, JA
Funding: YSH

Competing interests: All authors declare that they have no competing interests.

Code availability:

Custom MATLAB scripts are available on GitHub at https://github.com/nrams12/DBSCAN-Clusterer-NND-MaximaCD81.

Figures and Tables

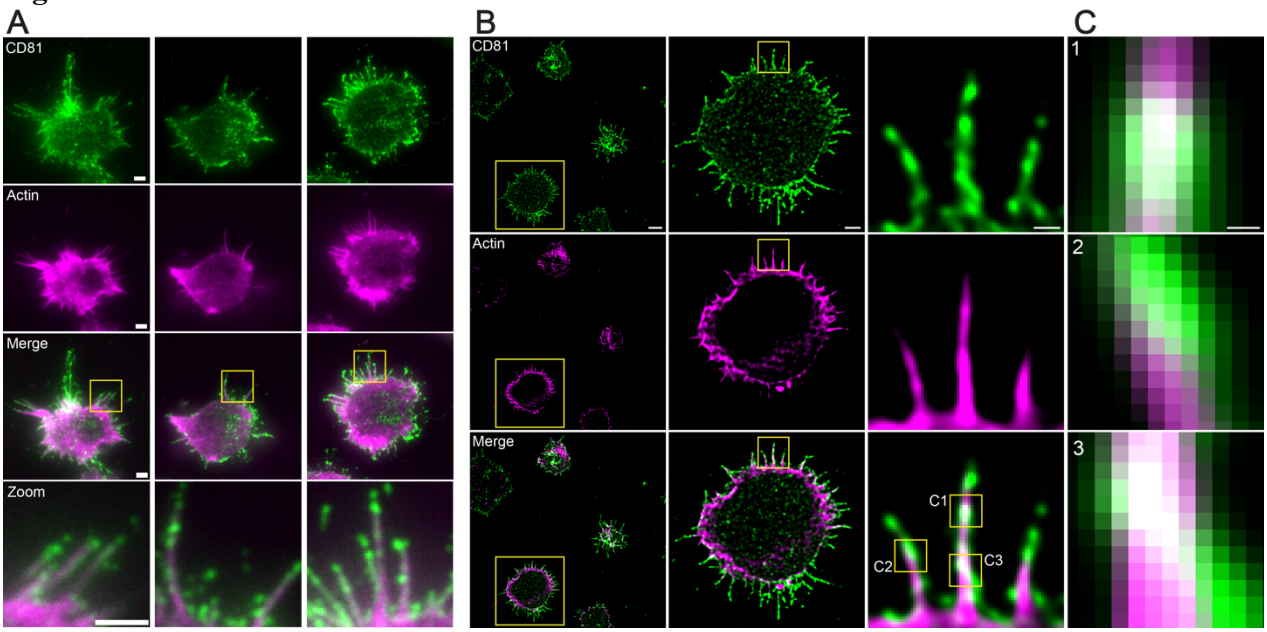

Figure 1: Fluorescence superresolution microscopy demonstrated CD81 localization on Jurkat T cell microvilli. (**A**) TIRF Immunofluorescence images of CD81 (green), F-actin (magenta), merged, and magnified views of the box in the merged images. (**B**) DeepSIM images of CD81 (green), F-actin (magenta), and merged. Magnified views shown from left to right. Arrows point to CD81 localization next to (solid filled arrow), on top of (hollow-tipped arrow), and wrapping around (fully hollow arrow) the F-actin fibers. (**C**) Magnified views of the regions in panel B showing differential localizations of CD81 in relation to F-actin: CD81 localization on top of (1), next to (2), and wrapping around (3) the F-actin fibers. Scale Bars: 5µm (**B left**), 2µm (**A, B middle**), 500 nm (**B right**) and 100 nm (**C**).

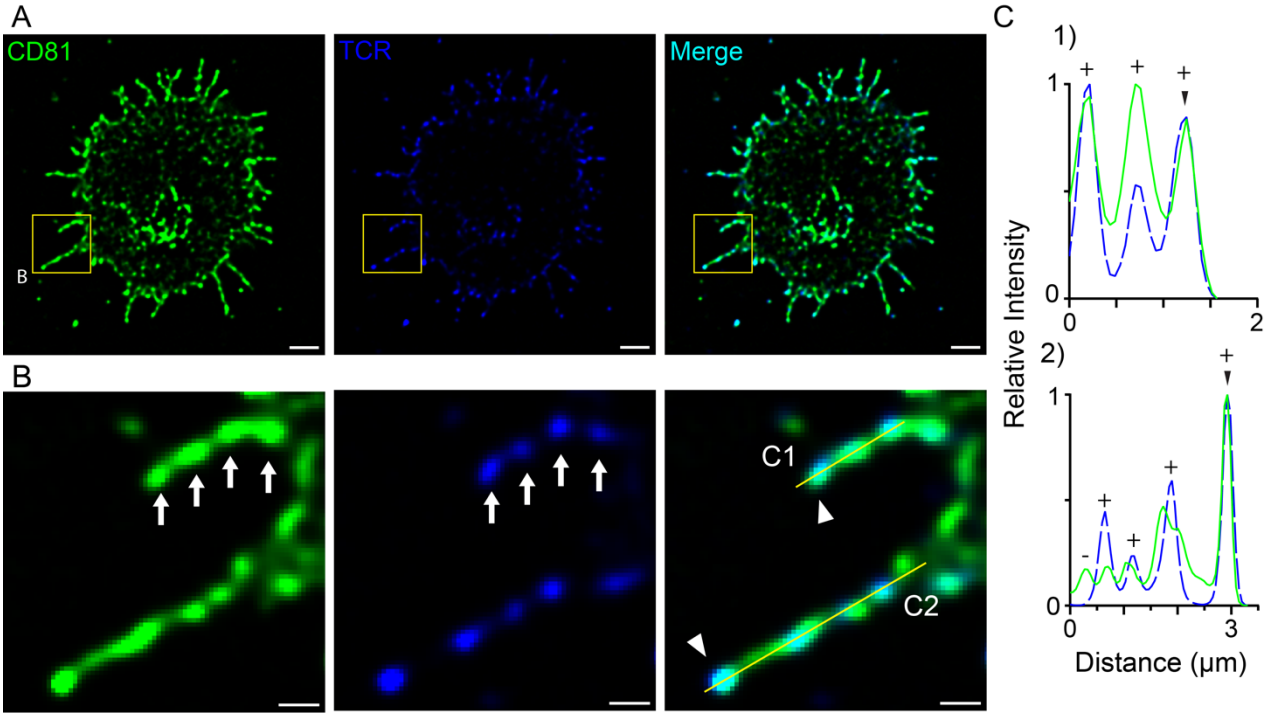

Figure 2: TCR colocalizes with CD81 on the microvilli. (**A**) DeepSIM image of CD81 (green) and TCR (blue) (**B**) Magnified views of two microvilli display colocalization of both CD81 and CD63 (teal) at the tips of the microvilli. (**C**) Line profiles displaying the relative intensity of CD81 (solid green) and TCR (dashed blue). (+) denotes where CD81 and TCR have peaks, and (–) denotes where CD81 peaks without TCR. Scale Bars: 2 μm (**A**), 500 nm (**B**,).

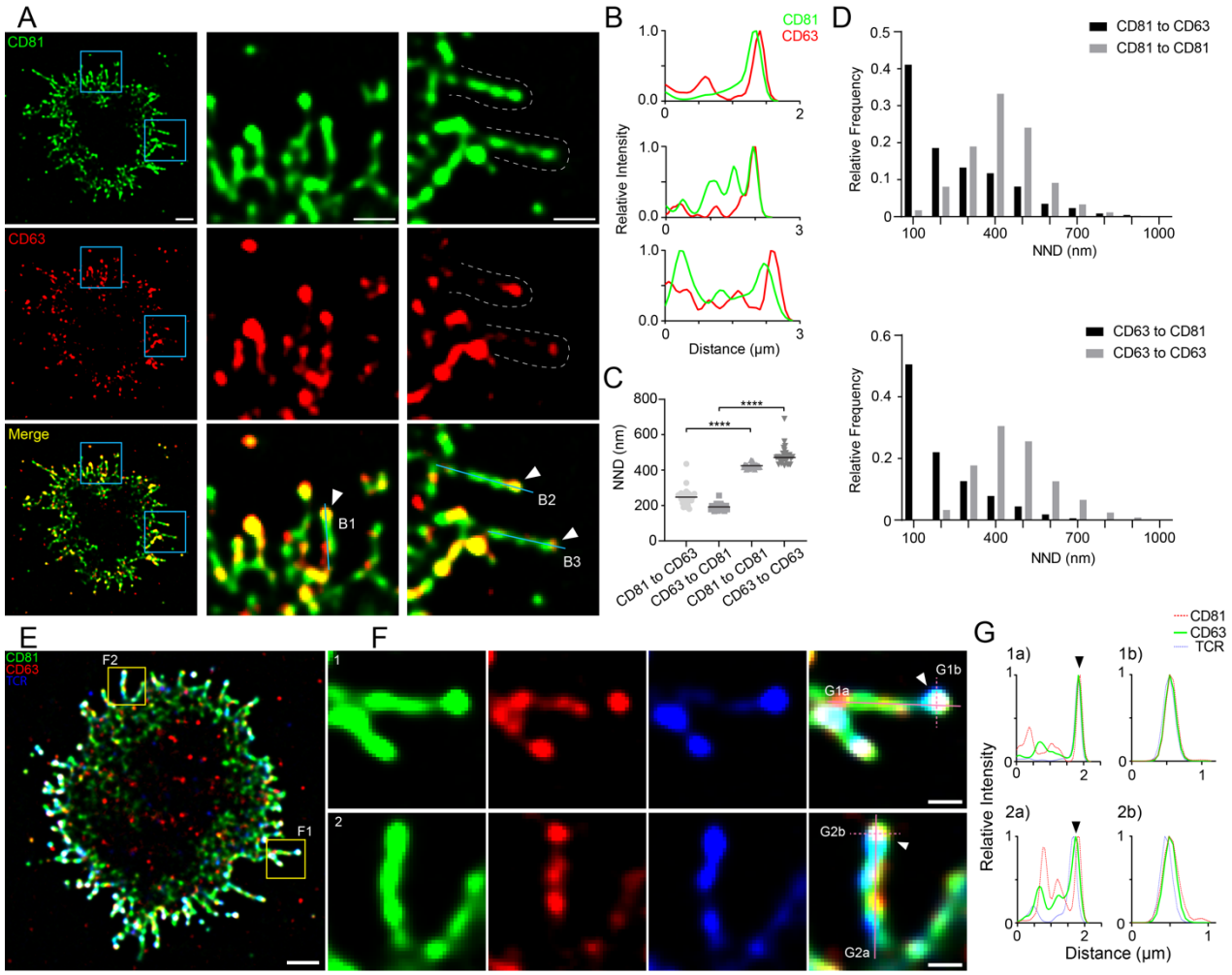

Figure 3: CD63 associates with CD81 and colocalizes with CD81 and TCR on microvilli tips. (**A**) DeepSIM images of CD81 (green) and CD63 (red) showing colocalization (yellow) at the tips of microvilli. (**B**) Line profiles of the lines in **A** showing colocalization of CD63 and CD81 at the tip of the microvillus. (**C**) Comparison of the NND of intensity maxima between CD81 and CD63 along the microvilli (n = 28). Bar displays the mean. Statistical significance was evaluated using a Student's t-test (**** $p < 0.0001$). (**D**) Histogram comparing NNDs: CD81 to CD63, CD81 to CD81 (top), CD63 to CD81, CD63 to CD63 (bottom). (**E**) DeepSIM image of CD81 (green), CD63 (red), and TCR (blue) (**F**) Magnified views of two microvilli display colocalization of all three channels (white) at the tips of the microvilli. (**G**) Line profiles displaying the relative intensity of CD81 (green solid), CD63 (red long-dashed), and TCR (blue short-dashed) corresponding to the lines in **F**. Scale Bars: 2 µm (**A** left, **E**), 500 nm (**A** middle & right, **F**).

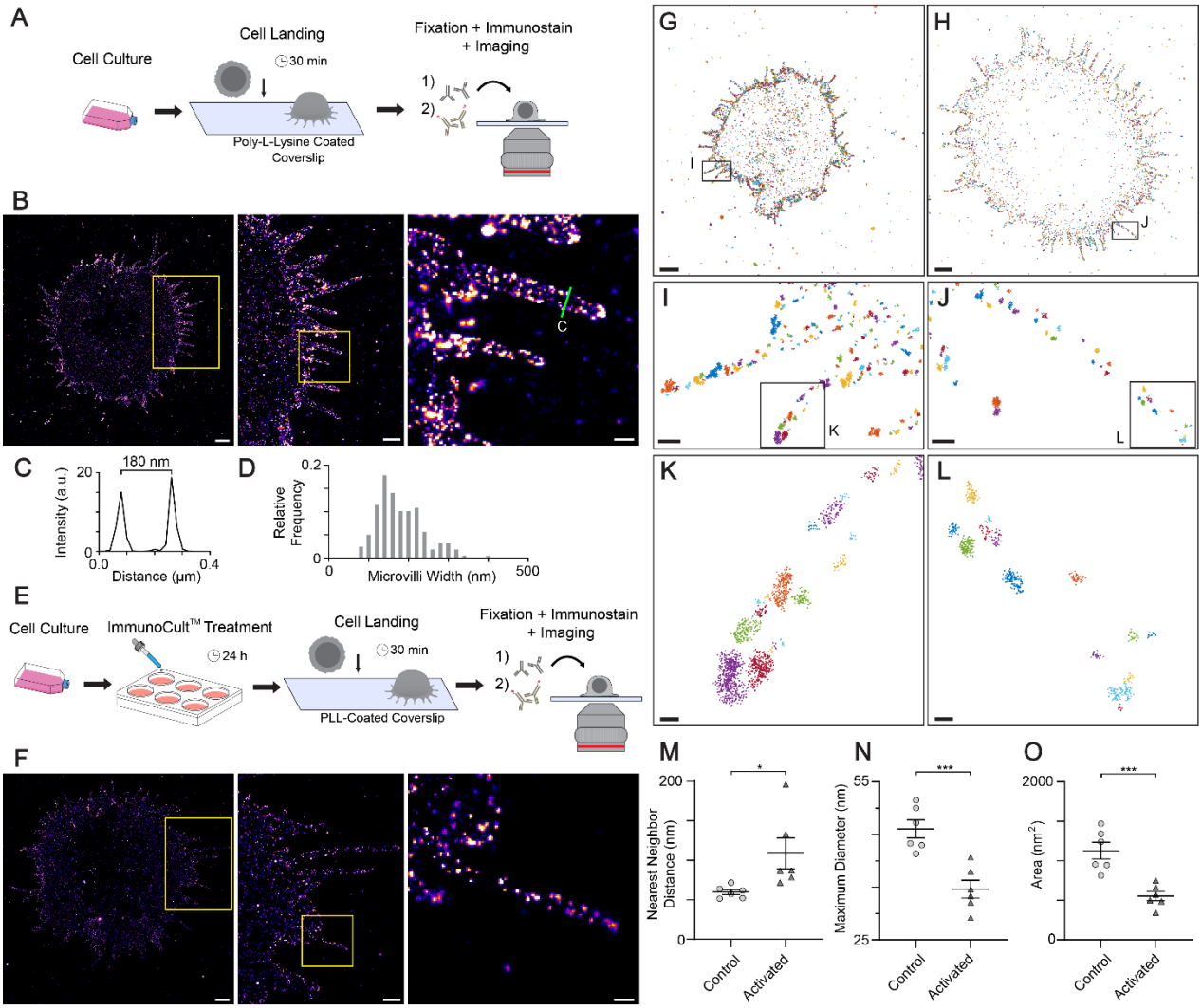

Figure 4: **CD81 *d*STORM imaging enables microvilli width measurement and reveals nanoscale clustering rearrangement on the microvilli after *in vitro* activation.** (**A**) Schematic depicting the landing, fixation, and immunostaining of untreated Jurkat cells for imaging. (**B**) *d*STORM image of a Jurkat cell with magnified views shown to the right. (**C**) The line profile shown in panel **B (right)**, depicting the width measurement. (**D**) Distribution of microvilli width measurements. (**E**) Schematic depicting ImmunoCult™ treatment, landing, fixation, and immunostaining of 24h activated Jurkat cells for imaging. (**F**) A *d*STORM image of a 24-h activated Jurkat cell, with magnified views shown to the right. (**G, H**) CD81 *d*STORM localizations clustered by DBSCAN on a control Jurkat cell (**G**) and a 24-h activated Jurkat cell (**H**). (**I**) Magnified view of the box shown in panel **G**. (**J**) Magnified view of the box shown in panel **H**. (**K**) Magnified view of the box indicated in panel **I**. (**L**) Magnified view of the box indicated in panel **J**. Comparison of the NND (**M**), maximum diameter (**N**), and cluster area (**O**) of CD81 clusters on the microvilli of control cells ($n = 6$) and 24-h activated cells ($n = 6$). Bar graphs display mean and SEM. Statistical significance was evaluated using a Student's *t*-test. ***$p<0.001$, *$p<0.05$. Scale Bars: 2 µm (**B(left), F(left), G, H**), 1 µm (**B(middle), F(middle)**), 250 nm (**B(right), F(right), I, J**), and 50 nm (**K, L**).

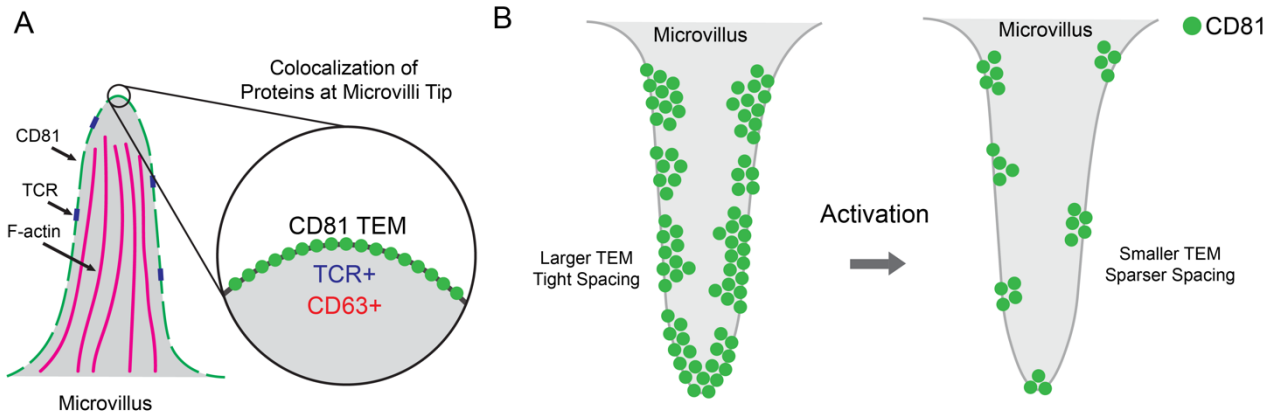

Figure 5: CD81 colocalization with CD63 and TCR on the tip of actin-rich Jurkat T cell microvilli and CD81 rearrangements after *in vitro* activation. (**A**) Illustration depicting TEMs of CD81 along the actin rich microvilli. The magnified view of the microvilli tip shows CD81 TEM colocalize with CD63 and TCR. (**B**) Illustration depicting the spatial rearrangement of CD81 on the microvilli of Jurkat T cells after activation, highlighting a reduction in domain size and an increase in domain separation.

Supplementary Materials

Please see Supplementary Materials Document.

References

1. S. Levy, T. Shoham, Protein-protein interactions in the tetraspanin web. *Physiology (Bethesda)* **20**, 218–224 (2005).

2. E. Rubinstein, F. Le Naour, C. Lagaudrière-Gesbert, M. Billard, H. Conjeaud, C. Boucheix, CD9, CD63, CD81, and CD82 are components of a surface tetraspan network connected to HLA-DR and VLA integrins. *Eur. J. Immunol.* **26**, 2657–2665 (1996).

3. M. Zuidscherwoude, F. Göttfert, V. M. E. Dunlock, C. G. Figdor, G. van den Bogaart, A. B. van Spriel, The tetraspanin web revisited by super-resolution microscopy. *Sci. Rep.* **5**, 12201 (2015).

4. S. Levy, S. C. Todd, H. T. Maecker, CD81 (TAPA-1): a molecule involved in signal transduction and cell adhesion in the immune system. *Annu. Rev. Immunol.* **16**, 89–109 (1998).

5. M. E. Hemler, Specific tetraspanin functions. *J. Cell Biol.* **155**, 1103–1107 (2001).

6. X. A. Zhang, C. Huang, Tetraspanins and cell membrane tubular structures. *Cell. Mol. Life Sci.* **69**, 2843–2852 (2012).

7. R. Bari, Q. Guo, B. Xia, Y. H. Zhang, E. E. Giesert, S. Levy, J. J. Zheng, X. A. Zhang, Tetraspanins regulate the protrusive activities of cell membrane. *Biochem. Biophys. Res. Commun.* **415**, 619–626 (2011).

563 8. U. H. von Andrian, S. R. Hasslen, R. D. Nelson, S. L. Erlandsen, E. C. Butcher, A central
564 role for microvillous receptor presentation in leukocyte adhesion under flow. *Cell* **82**, 989–
565 999 (1995).

566 9. S. Majstoravich, J. Zhang, S. Nicholson-Dykstra, S. Linder, W. Friedrich, K. A. Siminovitch,
567 H. N. Higgs, Lymphocyte microvilli are dynamic, actin-dependent structures that do not
568 require Wiskott-Aldrich syndrome protein (WASp) for their morphology. *Blood* **104**, 1396–
569 1403 (2004).

570 10. A. Polliack, The contribution of scanning electron microscopy in haematology: its role in
571 defining leucocyte and erythrocyte disorders. *J. Microsc.* **123**, 177–187 (1981).

572 11. H.-R. Kim, Y. Mun, K.-S. Lee, Y.-J. Park, J.-S. Park, J.-H. Park, B.-N. Jeon, C.-H. Kim, Y.
573 Jun, Y.-M. Hyun, M. Kim, S.-M. Lee, C.-S. Park, S.-H. Im, C.-D. Jun, T cell microvilli
574 constitute immunological synaptosomes that carry messages to antigen-presenting cells. *Nat.*
575 *Commun.* **9**, 3630 (2018).

576 12. E. Cai, K. Marchuk, P. Beemiller, C. Beppler, M. G. Rubashkin, V. M. Weaver, A. Gérard,
577 T.-L. Liu, B.-C. Chen, E. Betzig, F. Bartumeus, M. F. Krummel, Visualizing dynamic
578 microvillar search and stabilization during ligand detection by T cells. *Science* **356**, eaal3118
579 (2017).

580 13. Y. Jung, I. Riven, S. W. Feigelson, E. Kartvelishvily, K. Tohya, M. Miyasaka, R. Alon, G.
581 Haran, Three-dimensional localization of T-cell receptors in relation to microvilli using a
582 combination of superresolution microscopies. *Proc. Natl. Acad. Sci. U. S. A.* **113**, E5916–
583 E5924 (2016).

584 14. J. C. Yi, L. E. Samelson, Microvilli set the stage for T-cell activation. *Proc. Natl. Acad. Sci.*
585 *U. S. A.* **113**, 11061–11062 (2016).

586 15. K. Choudhuri, J. Llodrá, E. W. Roth, J. Tsai, S. Gordo, K. W. Wucherpfennig, L. C. Kam, D.
587 L. Stokes, M. L. Dustin, Polarized release of T-cell-receptor-enriched microvesicles at the
588 immunological synapse. *Nature* **507**, 118–123 (2014).

589 16. E. I. Buzas, The roles of extracellular vesicles in the immune system. *Nat. Rev. Immunol.* **23**,
590 236–250 (2023).

591 17. B. Fritzsching, B. Schwer, J. Kartenbeck, A. Pedal, V. Horejsi, M. Ott, Release and
592 intercellular transfer of cell surface CD81 via microparticles. *J. Immunol.* **169**, 5531–5537
593 (2002).

594 18. V. Rocha-Perugini, M. Zamai, J. M. González-Granado, O. Barreiro, E. Tejera, M. Yañez-
595 Mó, V. R. Caiolfa, F. Sanchez-Madrid, CD81 controls sustained T cell activation signaling
596 and defines the maturation stages of cognate immunological synapses. *Mol. Cell. Biol.* **33**,
597 3644–3658 (2013).

598 19. S. I. Cevik, N. Keskin, S. Belkaya, M. I. Ozlu, E. Deniz, U. H. Tazebay, B. Erman, CD81
599 interacts with the T cell receptor to suppress signaling. *PLoS One* **7**, e50396 (2012).

600 20. S. C. Todd, S. G. Lipps, L. Crisa, D. R. Salomon, C. D. Tsoukas, CD81 expressed on human
601 thymocytes mediates integrin activation and interleukin 2-dependent proliferation. *J. Exp.*
602 *Med.* **184**, 2055–2060 (1996).

603 21. T. Imai, O. Yoshie, C33 antigen and M38 antigen recognized by monoclonal antibodies
604 inhibitory to syncytium formation by human T cell leukemia virus type 1 are both members
605 of the transmembrane 4 superfamily and associate with each other and with CD4 or CD8 in
606 T cells. *J. Immunol.* **151**, 6470–6481 (1993).

607 22. T. Imai, M. Kakizaki, M. Nishimura, O. Yoshie, Molecular analyses of the association of
608 CD4 with two members of the transmembrane 4 superfamily, CD81 and CD82. *J. Immunol.*
609 **155**, 1229–1239 (1995).

610 23. Y. Sagi, A. Landrigan, R. Levy, S. Levy, Complementary costimulation of human T-cell
611 subpopulations by cluster of differentiation 28 (CD28) and CD81. *Proc. Natl. Acad. Sci. U.*
612 *S. A.* **109**, 1613–1618 (2012).

613 24. D. A. Witherden, R. Boismenu, W. L. Havran, CD81 and CD28 costimulate T cells through
614 distinct pathways. *J. Immunol.* **165**, 1902–1909 (2000).

615 25. C. T. Tseng, E. Miskovsky, G. R. Klimpel, Crosslinking CD81 results in activation of
616 TCRgammadelta T cells. *Cell. Immunol.* **207**, 19–27 (2001).

617 26. H. Gunasekara, T. Perera, C.-J. Chao, J. Bruno, B. Saed, J. Anderson, Z. Zhao, Y. S. Hu,
618 Phalloidin-PAINT: Enhanced quantitative nanoscale imaging of F-actin. *Biophys. J.* **123**,
619 3051-3064 (2024).

620 27. K. E. Keller, J. M. Bradley, Y. Y. Sun, Y.-F. Yang, T. S. Acott, Tunneling nanotubes are
621 novel cellular structures that communicate signals between trabecular meshwork cells.
622 *Invest. Ophthalmol. Vis. Sci.* **58**, 5298 (2017).

623 28. M. Chang, O.-C. Lee, G. Bu, J. Oh, N.-O. Yunn, S. H. Ryu, H.-B. Kwon, A. B. Kolomeisky,
624 S.-H. Shim, J. Doh, J.-H. Jeon, J.-B. Lee, Formation of cellular close-ended tunneling
625 nanotubes through mechanical deformation. *Sci. Adv.* **8**, eabj3995 (2022).

626 29. Q. Li, A. Lau, T. J. Morris, L. Guo, C. B. Fordyce, E. F. Stanley, A syntaxin 1, Galpha(o),
627 and N-type calcium channel complex at a presynaptic nerve terminal: analysis by
628 quantitative immunocolocalization. *J. Neurosci.* **24**, 4070–4081 (2004).

629 30. M. E. Hemler, Targeting of tetraspanin proteins — potential benefits and strategies. *Nat.*
630 *Rev. Drug Discov.* **7**, 747–758 (2008).

631 31. S. Charrin, F. le Naour, O. Silvie, P.-E. Milhiet, C. Boucheix, E. Rubinstein, Lateral
632 organization of membrane proteins: tetraspanins spin their web. *Biochem. J.* **420**, 133–154
633 (2009).

634 32. Y. Jung, L. Wen, A. Altman, K. Ley, CD45 pre-exclusion from the tips of T cell microvilli
635 prior to antigen recognition. *Nat. Commun.* **12**, 3872 (2021).

636 33. S. C. Schmidt, A. Massenberg, Y. Homsi, D. Sons, T. Lang, Microscopic clusters feature the
637 composition of biochemical tetraspanin-assemblies and constitute building-blocks of
638 tetraspanin enriched domains. *Sci. Rep.* **14**, 2093 (2024).

639 34. S. J. Israels, E. McMillan-Ward, Platelet tetraspanin complexes and their association with
640 lipid rafts. *Thromb. Haemost.* **98**, 1081–1087 (2007).

641 35. K. Pfistershammer, O. Majdic, J. Stöckl, G. Zlabinger, S. Kirchberger, P. Steinberger, W.
642 Knapp, CD63 as an activation-linked T cell costimulatory element. *J. Immunol.* **173**, 6000–
643 6008 (2004).

644 36. S. van de Linde, A. Löschberger, T. Klein, M. Heidbreder, S. Wolter, M. Heilemann, M.
645 Sauer, Direct stochastic optical reconstruction microscopy with standard fluorescent probes.
646 *Nat. Protoc.* **6**, 991–1009 (2011).

647 37. M. Heilemann, S. van de Linde, M. Schüttpelz, R. Kasper, B. Seefeldt, A. Mukherjee, P.
648 Tinnefeld, M. Sauer, Subdiffraction-resolution fluorescence imaging with conventional
649 fluorescent probes. *Angew. Chem. Int. Ed Engl.* **47**, 6172–6176 (2008).

650 38. K. Lange, Fundamental role of microvilli in the main functions of differentiated cells:
651 Outline of an universal regulating and signaling system at the cell periphery. *J. Cell. Physiol.*
652 **226**, 896–927 (2011).

653 39. Ester, M., Kriegel, H.-P., Sander, J. & Xu, X. A density-based algorithm for discovering
654 clusters in large spatial databases with noise. *kdd* **96**, 226–231 (1996).

655 40. O. V. Kovalenko, X. Yang, T. V. Kolesnikova, M. E. Hemler, Evidence for specific
656 tetraspanin homodimers: inhibition of palmitoylation makes cysteine residues available for
657 cross-linking. *Biochem. J.* **377**, 407–417 (2004).

658 41. Y. Homsi, J.-G. Schloetel, K. D. Scheffer, T. H. Schmidt, N. Destainville, L. Florin, T. Lang,
659 The extracellular δ-domain is essential for the formation of CD81 tetraspanin webs. *Biophys.*
660 *J.* **107**, 100–113 (2014).

661 42. L. Querol Cano, V.-M. E. Dunlock, F. Schwerdtfeger, A. B. van Spriel, Membrane
662 organization by tetraspanins and galectins shapes lymphocyte function. *Nat. Rev. Immunol.*
663 **24**, 193–212 (2024).

664 43. C. Huang, C. Fu, J. D. Wren, X. Wang, F. Zhang, Y. H. Zhang, S. A. Connel, T. Chen, X. A.
665 Zhang, Tetraspanin-enriched microdomains regulate digitation junctions. *Cell. Mol. Life Sci.*
666 **75**, 3423–3439 (2018).

667 44. S. Nydegger, S. Khurana, D. N. Krementsov, M. Foti, M. Thali, Mapping of tetraspanin-
668 enriched microdomains that can function as gateways for HIV-1. *J. Cell Biol.* **173**, 795–807
669 (2006).

670 45. J. He, E. Sun, M. V. Bujny, D. Kim, M. W. Davidson, X. Zhuang, Dual function of CD81 in
671 influenza virus uncoating and budding. *PLoS Pathog.* **9**, e1003701 (2013).

672 46. M. L. Shaw, K. L. Stone, C. M. Colangelo, E. E. Gulcicek, P. Palese, Cellular proteins in
673 influenza virus particles. *PLoS Pathog.* **4**, e1000085 (2008).

674 47. E. G. Cormier, F. Tsamis, F. Kajumo, R. J. Durso, J. P. Gardner, T. Dragic, CD81 is an entry
675 coreceptor for hepatitis C virus. *Proc. Natl. Acad. Sci. U. S. A.* **101**, 7270–7274 (2004).

676 48. J. A. McKeating, L. Q. Zhang, C. Logvinoff, M. Flint, J. Zhang, J. Yu, D. Butera, D. D. Ho,
677 L. B. Dustin, C. M. Rice, P. Balfe, Diverse hepatitis C virus glycoproteins mediate viral
678 infection in a CD81-dependent manner. *J. Virol.* **78**, 8496–8505 (2004).

679 49. M. Mittelbrunn, M. Yáñez-Mó, D. Sancho, A. Ursa, F. Sánchez-Madrid, Cutting edge:
680 Dynamic redistribution of tetraspanin CD81 at the central zone of the immune synapse in
681 both T lymphocytes and APC. *J. Immunol.* **169**, 6691–6695 (2002).

682 50. M. Ovesný, P. Křížek, J. Borkovec, Z. Svindrych, G. M. Hagen, ThunderSTORM: a
683 comprehensive ImageJ plug-in for PALM and STORM data analysis and super-resolution
684 imaging. *Bioinformatics* **30**, 2389–2390 (2014).